ROYAL SOCIETY
OF CHEMISTRY

## PAPER

# Enhancing thermometric efficiency: a wavelength excitation analysis in LiSrGdW$_3$O$_{12}$:Tb$^{3+}$ for superior single band ratiometric (SBR) thermometry

Fadwa Ayachi,[a] Kamel Saidi, [ID] [a] Mohamed Dammak, [ID] *[a] Joan Josep Carvajal [ID] [b] and Maria Cinta Pujol[b]

This study delves into the Single Band Ratiometric (SBR) method for luminescence thermometry, specifically employing Tb$^{3+}$-doped LiSrGdW$_3$O$_{12}$ (LSGW) as a novel phosphor. The prepared samples crystallize with the tetragonal scheelite structure, with the optimal Tb$^{3+}$ concentration pinpointed at 0.3Tb$^{3+}$ ions. When stimulated at diverse wavelengths exhibit luminescence characterized by varying heat dependencies. By utilizing two Fluorescence Intensity Ratio (FIR) parameters for the 544 nm green emission, firstly excited at 405 nm and 488 nm, and then at 405 nm and 379 nm, the $S_r$ relative thermal sensitivity of the luminescent thermometer peaks at 3.56% K$^{-1}$ and 4.21% K$^{-1}$, respectively, within the temperature range of 290–440 K. The temperature resolution ($\delta T$) of the luminescent thermometer is calculated to be $\delta T_1 = 0.68$ K and $\delta T_2 = 0.75$ K for $T = 290$ K, respectively. These outcomes underscore the applicability of Tb$^{3+}$ ions for SBR thermometry, emphasizing the impact of the excitation wavelength on the thermal sensitivity. The study lays the groundwork for developing highly sensitive temperature probes by elucidating the interplay of material properties and physical processes.

## 1. Introduction

It has been observed that research devoted to optimizing luminescent thermometry and charting new development avenues has grown in popularity as this technology provides a remote temperature readout with high resolution and sensitivity.[1–3] A single-band ratiometric (SBR) thermometer is one of the new approaches in luminescent thermometry that has recently received a lot of attention. It uses a single optically active center that is excited in two different ways, resulting in emission signals with opposite temperature dependences.[4–7] One of the major benefits of SBR luminescence thermometry is that the emission is only gathered in the selected spectral region. This allows us to prevent the negative impacts of selective absorption of a tested medium, which can change the shape of the emission spectrum and hence the reliability of the temperature readout. To achieve opposite thermal monotonicity of a single emission band, two primary excitation processes are utilized, namely edge excitation and excited state absorption. Because the latter allows for more extensive adjustment of the phosphor's thermographic characteristics, it is used more frequently. Lanthanide ions are the most ideal

kind of optically active centers to employ for this purpose because of their unique energy level distribution, which gives numerous options for selecting the right excitation wavelengths for SBR.[7–10] The intensity of the emission from these ions shows quenching as the temperature rises when they are activated at a resonant wavelength that matches the ground state absorption (GSA). However, when the excitation is matched to the excited state absorption (ESA), they also show a thermally driven rise in emission intensity under the right circumstances. The potential relative thermal sensitivity ($S_r$) of this kind of luminescent thermometer is greatly increased by the fluctuation of GSA and ESA stimulated emission intensity. Results that were recently published demonstrated how the kind of doping ion, the nature of the host material, and the interionic energy transfer affect the thermally induced ESA process.[4,5] Nonetheless, up to now, the focus has been on process improvement that results in the thermal enhancement of the ESA process.

The selection of an appropriate host material is pivotal in the design of high-efficiency luminescent materials and high-performance luminescent sensors. Inorganic luminescent materials play a critical role in contemporary photonics technologies. Among these, binary alkaline earth tungstates, represented by the formula MLn$_2$(WO$_4$)$_4$ (where M denotes an alkaline earth bivalent metal ion, and Ln represents trivalent rare-earth ions), are classified as scheelite-structured compounds. The scheelite structure is prevalent in binary molybdates and tungstates, and noteworthy reports underscore their exceptional upconversion (UC) photoluminescence

*aLaboratoire de Physique Appliquée, Groupe des Matériaux Luminescents, Faculté des Sciences de Sfax, Département de Physique, Université de Sfax, BP, 1171, Sfax, Tunisia. E-mail: madidammak@yahoo.fr; Mohamed.dammak@fss.usf.tn*

*bUniversitat Rovira i Virgili, Departament de Química Física i Inorgànica, Materials in Green Chemistry (GreenMat), Marcel·li Domingo 1, Tarragona 43007, Spain*

properties.[11,12] Tungstate compounds are widely recognized as essential inorganic functional materials with a rich history of practical applications in scintillation detectors, solid-state lasers, and stimulated Raman scattering (SRS). For instance, crystals like $PbWO_4$ and $CdWO_4$ exhibit excellent scintillation properties.[6] Additionally, $KGd(WO_4)_2$:Nd (KGW:Nd) and $KY(WO_4)_2$:Nd (KYW:Nd) crystals have demonstrated competitive properties with commercial Nd:YAG crystals in quasi-CW and Q-switched lasers due to their short storage time and large emission cross-sections.[7] Furthermore, certain tungstate crystals, such as KGW and $BaWO_4$,[15,16] showcase significant third-order nonlinearities and have been explored as promising Raman shifters. On the flip side, ternary tungstates with a general composition of $NaMLn(WO_4)_3$ (M = $Ca^{3+}$, $Sr^{3+}$, and $Ba^{3+}$; Ln = $La^{3+}$, $Gd^{3+}$, and $Y^{3+}$), which crystallize in the monoclinic crystallographic system with the $C2/c$ space group, have been documented. Specifically, $NaSrLa_{1-x}(WO_4)_3$,[9] and $KBaGd(WO_4)_3$ have been identified as noteworthy instances, with the latter emerging as a novel host material for solid-state lasers.[18,19]

To date, SBR thermometry, relying on the emission of various lanthanide ions, has been successfully demonstrated, with predominant attention given to lanthanides such as $Tb^{3+}$, $Eu^{3+}$, or $Nd^{3+}$.[20–30] These ions, owing to their well-defined and intricate energy-level configurations, prove effective in conducting temperature measurements using the SBR approach. This involves excitations matched to both ground-state absorption (GSA) and excited-state absorption (ESA). The existing literature on SBR luminescent thermometers predominantly focuses on near-infrared (NIR) emissions, exemplified by $Nd^{3+}$,[28,29] or green-emitting phosphors, such as $Tb^{3+}$.[21,22,24,27,30] Additionally, investigations have extended to the red and yellow spectral ranges utilizing $Eu^{3+}$-doped phosphors.[20,23,25,26]

For optimal performance employing the SBR strategy to develop a high-performance luminescent sensor, this study places emphasis on evaluating the impact of the excitation wavelength on the thermometric parameters. In this article, $Tb^{3+}$-doped LSGW phosphors were synthesized through the conventional solid-state reaction method. Our focus is on the $LiSrGdW_3O_{12}$ (LSGW) host, chosen for its cost-effectiveness and ease of preparation. The results obtained indicate a promising direction for enhancing temperature sensing precision and sensitivity.

## 2. Equipment, synthesis and characterization

A series of terbium doped LSGW microcrystals $LiSrGd_{1-x}Tb_x(WO_4)_3$ ($x$ = 0.1, 0.2, 0.3, 0.4, 0.5 and 0.6) were prepared by solid state reaction. $Li_2CO_3$ (99.99%), $SrCO_3$ (99.99%), $Gd_2O_3$ (99.99%), $WO_3$ (99.99%) and $Tb_4O_7$ (99.99%) were used as starting materials.

The stoichiometric coefficient of $Li_2CO_3$, $SrCO_3$, $Gd_2O_3$, $WO_3$ and $Tb_4O_7$ were taken and ground using an agate mortar and pestle and calcined at 600 °C for 16 h and then reground, and annealed at 800 °C for 12 h. Finally, the collected phosphors

were ground again to produce a fine powder and were kept in the container for further analysis.

The X-ray powder diffraction (XRPD) of all synthesized phosphors was recorded using a SIEMENS D8-θ/2θ with a Cu Kα X-ray source ($\lambda$ = 0.15418 nm). The SEM images were taken with a Quanta 600 environmental scanning electron microscope (ESEM) from FEI. Diffuse reflection spectra were measured between 250 and 1100 nm with a scanning UV-Vis spectrophotometer (PerkinElmer). The photoluminescence spectra (excitation and emission) were recorded using a Horiba Fluoromax 4P spectrometer equipped with a Xenon lamp as the excitation source at room temperature. The sample temperature was controlled to be in the 300–440 K range by using a helium closed-cycle cryostat and a Lake Shore 321 temperature controller. The CIE colour coordinates were calculated from the emission spectral data of the synthesised phosphors using a chromaticity calculator program developed by ourselves.

## 3. Results and discussions

### 3.1 Crystalline and morphological characterization of the obtained products

Fig. 1a displays the XRPD patterns of the obtained products, denoted as $LiSrGd(WO_4)_3$:$x$%$Tb^{3+}$ (where $x$ = 10, 20, 30, 40, and 50). The predominant peak at $2\theta$ = 28.5° is accompanied by other peaks at 31°, 34°, 39°, 47°, 49°, 54°, 58°, 59°, and 76°, which closely match the reference pattern card JCPD S25-0829.[11] Table 1 presents the unit cell parameters corresponding to various Tb concentrations. The samples exhibit a crystalline structure consistent with orthorhombic scheelite, characterized by the space group $I4_1/a$ (no. 88).[11]

A maximum shift of $\theta \approx 18°$ was found for the lowest angle region, shown in the inset of Fig. 1, when the $Tb^{3+}$ concentration increased. Table 1 summarizes the unit cell parameters refined by using the Le Bail methodology using the TOPAS software.
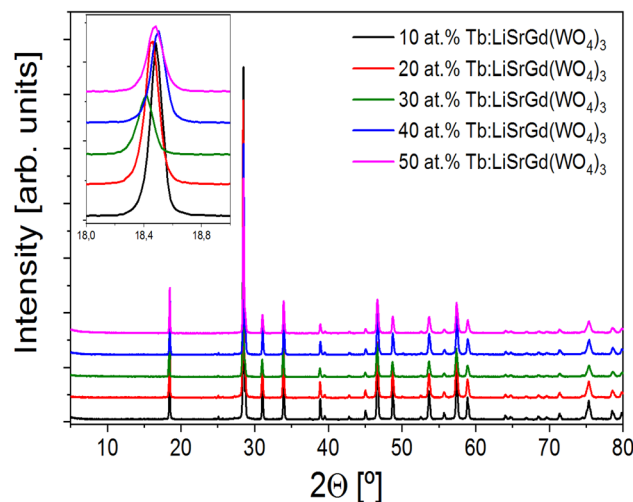


**Fig. 1** XRPD patterns of the obtained products, $x$% $Tb^{3+}$:$LiSrGd(WO_4)_3$ being $x$ = 10, 20, 30, 40 and 50. Inset: Angle shift related to the Tb concentration.

**Table 1** Evolution of the unit cell parameters as a function of the doping level. $R_{exp}$ equals to expected $R$ value and $R_{wp}$ equals to the weighted-profile $R$-value. Values of $R_{wp}/R_{exp}$ close to 1 indicates the good quality of the Le Bail fitting[12]

| % Tb | $a$ (Å) | $c$ (Å) | Volume (Å³) | $R_{exp}/R_{wp}$ |
|------|---------|---------|-------------|------------------|
| 10 | 5.28349(8) | 11.5189(2) | 321.553(12) | 4.51/7.49 |
| 20 | 5.28165(10) | 11.5138(2) | 321.189(14) | 4.60/6.96 |
| 30 | 5.27709(13) | 11.5007(3) | 320.269(18) | 6.01/7.88 |
| 40 | 5.28214(11) | 11.5145(3) | 321.268(16) | 5.18/7.99 |
| 50 | 5.28121(14) | 11.5146(3) | 321.154(19) | 5.73/8.06 |

The introduction of $Tb^{3+}$ into the crystalline structure results in a reduction of the unit cell parameters. This phenomenon can be attributed to the disorder arising from the $Gd^{3+} \rightarrow Tb^{3+}$ substitution. The incorporation of $Tb^{3+}$ ions into the LSGW lattice induces a local distortion of the crystal structure. The anticipated compression during the substitution of $Gd^{3+}$ by $Tb^{3+}$ is attributed to the difference in ionic radii, specifically, the coordination 8 radii of $Gd^{3+}$ (1.053 Å) and $Tb^{3+}$ (1.040 Å).

The SEM photographs presented in Fig. 2 illustrate the shape, size and distribution of the particles in the samples. SEM images showed that the particles are micrometric in size, without significant changes in morphology when the concentration of $Tb^{3+}$ increased.

### 3.2 Optical characterizations

**3.2.1 UV-vis absorption.** The diffuse reflectance spectra (Fig. 3) of LSGW:$x$Tb$^{3+}$ phosphors ($x$ = 0.1, 0.2, 0.3, 0.4, and 0.6) over the range 200–1100 nm are shown in Fig. 3.

In this spectra, the electronic transitions corresponding to the group $(WO_4)^{2-}$ are the origin of a wide band with the highest intensity in the 240–370 nm range.[13] The optical band gaps ($E_g$) of the prepared phosphors have been calculated from the diffuse reflection spectra, which may be determined by using the Kubelka–Munk (KM) and the Tauc equation.[14] Fig. 4 displays the plot of $(F(R)h\nu)^2$ *versus* $(h\nu)$, in which $F(R)$ is the reflection function measured. The LSGW:$x$Tb$^{3+}$ energy gap values were calculated to be: (a) $E_g$ = 3.02, (b) $E_g$ = 3.00, (c) $E_g$ = 2.98, (d) $E_g$ = 2.97, (e) $E_g$ = 2.95 and (f) $E_g$ = 2.93 eV for $x$ = 0.1, 0.2, 0.3, 0.4, 0.5 and 0.6 respectively. These values are lower than the ones obtained for $LiGd(WO_4)_2$, in which the direct optical
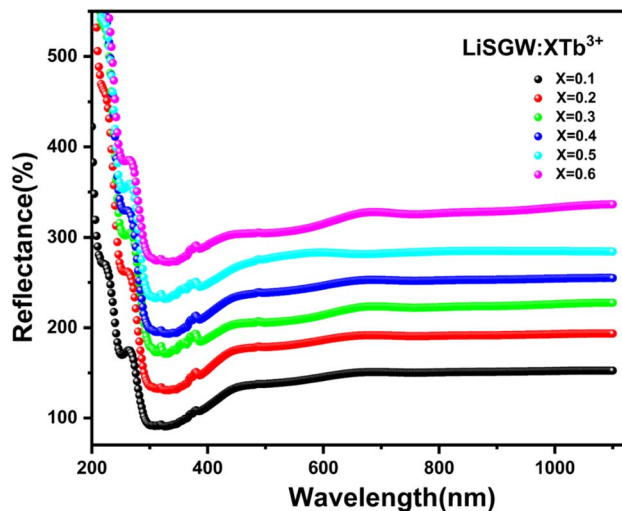


**Fig. 3** Diffuse reflectance spectra of LSGW:$x$Tb$^{3+}$ ($x$ = 0.1, 0.2, 0.3, 0.4, 0.5 and 0.6).

band gap observed was 3.607 eV. Therefore, the introduction of Tb in the crystalline structure reduces the band gap. Besides, the energy gap decreases from 3.02 to 2.93 eV as the doping content increases.

**3.2.2 Photoluminescence properties.** Fig. 5a presents the excitation spectrum (PLE) of LSGW:0.3Tb$^{3+}$ microcrystals, which was measured by monitoring the emission at 544 nm. The PLE shows a broad band located in the range of 250–305 nm and centered at 270 nm, which is attributed to the $O^{2-}-WO_4^{2-}$ charge transfer band (CTB) and f–d transition of $Tb^{3+}$, indicating the energy transfer from the matrix state (host) to $Tb^{3+}$ in LSGW:Tb$^{3+}$ phosphor.[15,16] A pronounced PLE band at 285 nm is observed for the $^8S_{7/2}/^6I_J$ intra-f–f transitions of $Gd^{3+}$, along with a less prominent band at 312 nm for the $^8S_{7/2}/^6P_J$ transitions.[17] These findings suggest that energy transfer from $Gd^{3+}$ to $Tb^{3+}$ is occurring. In the spectral range 330–500 nm, various excitation bands are seen which are allocated to intrinsic f–f transitions of $Tb^{3+}$ ions. Those peaks situated at about 352 nm, 359 nm, 369 nm, 379 nm and 486 nm correspond to the electronic transitions $^7F_6 \rightarrow {}^5D_2$, $^7F_6 \rightarrow {}^5G_5 + {}^5L_9$, $^7F_6 \rightarrow {}^5L_{10}$, $^7F_6 \rightarrow {}^5D_3 + {}^5G_6$, and $^7F_6 \rightarrow {}^5D_4$, respectively.[18] Fig. 5b displays the emission spectrum (PL) at room temperature of LSGW:0.3Tb$^{3+}$ under
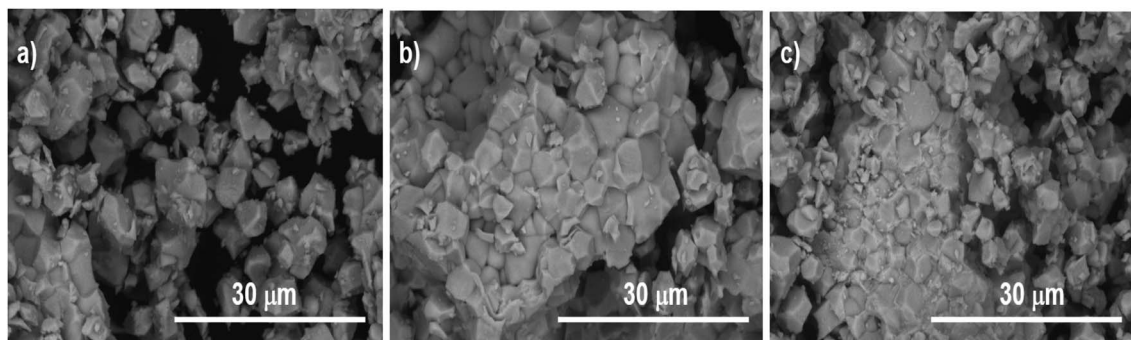


**Fig. 2** Scanning electron microscopy images of LSGW doped (a) 0.1Tb$^{3+}$, (b) 0.3Tb$^{3+}$, and (c) 0.5Tb$^{3+}$.
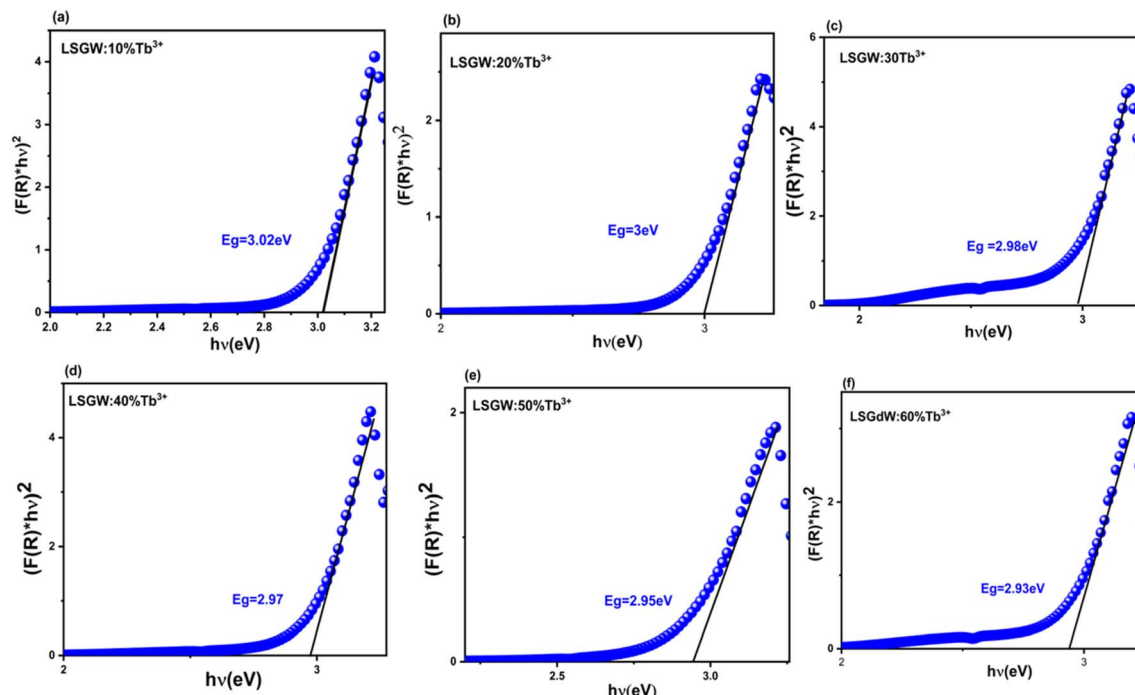
**Fig. 4** Plot of $[F(R)h\nu]^2$ versus $(h\nu)$ of LSGW doped with (a) 0.1, (b) 0.2, (c) 0.3, (d) 0.4, (e) 0.5 and (f) 0.6 $Tb^{3+}$, respectively.
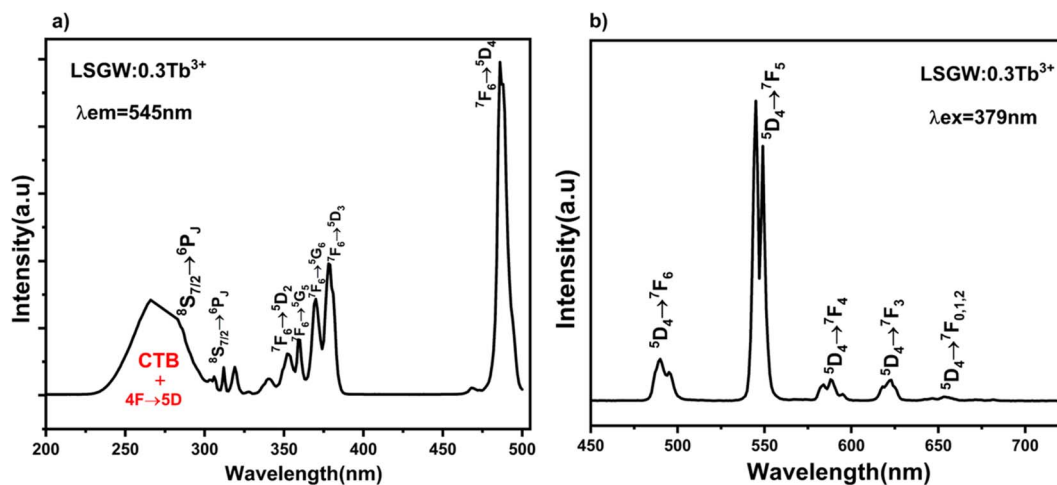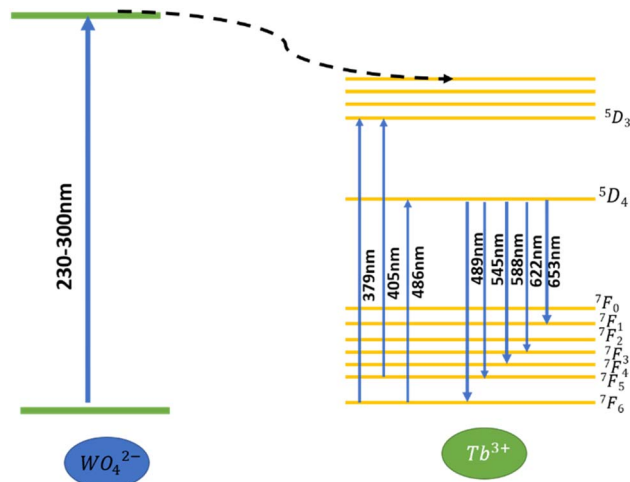


**Fig. 5** Room temperature (a) PLE and (b) PL spectra of LSGW:0.3$Tb^{3+}$.

379 nm excitation in the spectral range 450–750 nm. This spectrum showed a number of peaks at 489, 545, 588, 622 and 653 nm, which correspond to $Tb^{3+}$:$^5D_4 \rightarrow {}^7F_J$ transitions ($J = 6, 5, 4, 3$)[1,2] respectively. The energy diagram of the $(WO_4)^{2-}$ and $Tb^{3+}$ ions are presented in Fig. 6 to illustrate the photoluminescence and excitation processes in these materials.

In most cases, the emission intensity of lanthanide ion doped materials is mostly defined by the concentration of dopants. The emission spectra of LSGW doped with various concentrations of $Tb^{3+}$ ions ($x = 0.1, 0.2, 0.3, 0.4, 0.5$ and $0.6$) are presented in Fig. 7a. All the emission spectra exhibit the same form with a change in their intensities with an increase in the

$Tb^{3+}$ concentration. It is clear from the box that as the content of $Tb^{3+}$ ions increase, the emission intensity of $Tb^{3+}$ progressively increases and attains a maximum at $x = 0.3$. With higher $Tb^{3+}$ concentrations, the emission intensity decreases owing to the concentration quenching. It can be assigned to a non-radiative energy transfer between $Tb^{3+}$ ions. The nonradiative energy transfer could either be caused by a multipole–multipole interaction or an exchange interaction. In addition, the energy transfer between $Tb^{3+}$–$Tb^{3+}$ ions can be influenced mainly by the distances between the activator ions in the host matrix. The critical transfer distance $R_c$ calculated by Blasse's equation can be found by using the following expression (eqn (1)).[19,20]

**Fig. 6** Energy diagram of LSGW:0.3Tb$^{3+}$.

$$R_c = 2\left(\frac{3V}{4\pi N X_c}\right)^{1/3} \tag{1}$$

wherein $V$ is the unit cell volume, $N$ the number of cation sites for the dopant in a unit cell and $X_c$ is the critical concentration for the activator ion. In this case, $V = 320, 44$ cm$^{-1}$, $N = 4$ and $X_c = 0.3$, Therefore, the critical distance $(R_c)$ was calculated to be around 8 Å, which is above 5 Å. Based on the Dexter theory,[21] the mechanism of energy transfer can be controlled by a multipole–multipole interaction. Van Uitert's theory suggests that concentration quenching occurs due to interactions between the luminescent centers at high concentrations. The basic relationship between luminescence intensity and concentration can be expressed as:

$$\frac{1}{X} = K\left(1 + \frac{\beta(X)\theta}{3}\right)^{-1} \tag{2}$$

$\theta$ represents the multipole interaction constant equivalent to 6, 8 or 10 corresponding to dipole–dipole (D–D), dipole–

quadrupole (D–Q) and quadrupole–quadrupole (Q–Q) interactions, respectively. $K$ and $\beta$ are constants for each interaction upon the same excitation. Eqn (2) can be expanded as follows:

$$\log\frac{I}{X} = -\frac{\theta}{3}\log(X) + A \tag{3}$$

in which $A$ is a constant.

The straight-line relationship between $\log X$ and $\log(I/X)$ values of $x$Tb$^{3+}$ ($x = 0.1, 0.2, 0.3, 0.4, 0.5$ and $0.6$) doped phosphors is illustrated in Fig. 7b. The "$\theta$" value is near 6, indicating that the quenching phenomenon between the Tb$^{3+}$ ions in our LSGW compound corresponds to dipole–dipole (D–D) interactions.[22]

To estimate the luminous colour of the phosphor material, the CIE chromaticity coordinates, which are relevant for the
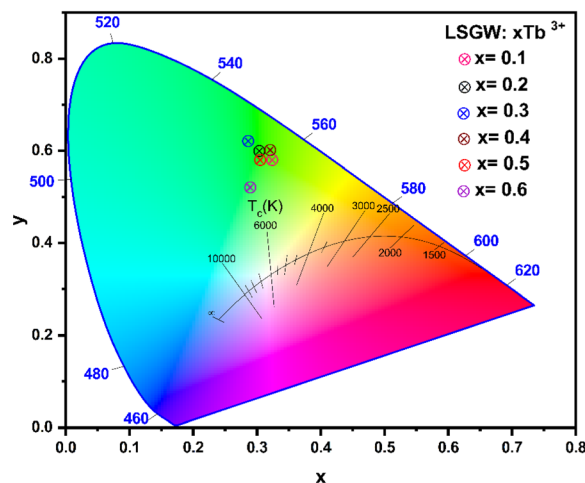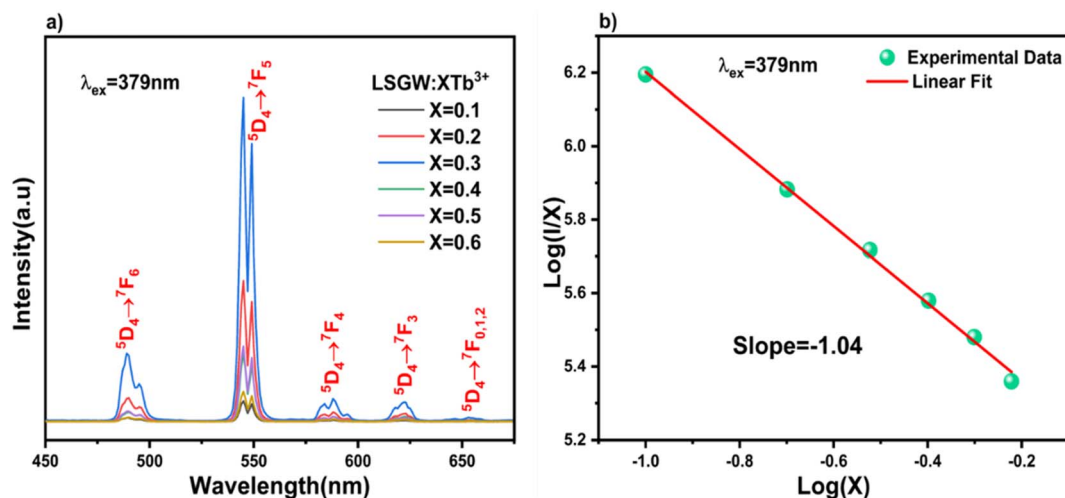


**Fig. 8** CIE chromaticity diagram at different concentration of LSGW:$x$Tb$^{3+}$ ($x = 0.1, 0.2, 0.3, 0.4, 0.5$ and $0.6$) phosphor. As we use the same symbol, it cannot be seen the change of the CIE coordinates with the Tb concentration.



**Fig. 7** (a) PL spectra of LSGW:$x$Tb$^{3+}$ ($x = 0.1, 0.2, 0.3, 0.4, 0.5$ and $0.6$) excited at 379 nm. (b) Linear fitting of log($I/X$) in terms of log($X$).

**Table 2** CIE 1931 chromaticity index for LiSrGdW$_3$O$_{12}$:$x$Tb$^{3+}$ ($x$ = 0.1–0.6) phosphors

| Samples | CIE ($x, y$) |
| --- | --- |
| $x$ = 0.1 | (0.30; 0.60) |
| $x$ = 0.2 | (0.30; 0.59) |
| $x$ = 0.3 | (0.32; 0.61) |
| $x$ = 0.4 | (0.30; 0.60) |
| $x$ = 0.5 | (0.31; 0.59) |
| $x$ = 0.6 | (0.31; 0.58) |

performance of the phosphors, were determined from emission spectra (see Fig. 8) The values that were calculated are given in Table 1. It is apparent that the colour coordinates of the LSGW:$x$Tb$^{3+}$ phosphors are in the red region of the CIE diagram. These results indicated that Tb$^{3+}$ doped LSGW phosphors could be a potential candidate for green LED application (Table 2).

# 4. Single-band ratiometric (SBR) approach thermometry

To investigate the optical thermal sensing behaviour of the as-prepared LSGW:Tb$^{3+}$ MCs, the emission spectra upon ESA and GSA were recorded at different temperatures. With its

wavelength-dependent thermal behaviour, Tb$^{3+}$ luminescence offers a great opportunity for SBR thermometry. As a result, the wavelengths of 379 nm and 486 nm were selected as GSA and 405 nm as ESA for the SBR model. Accordingly, the luminescence arising from the $^5$D$_4$–$^7$F$_5$ transition can be used as a sensitive thermometric parameter, since it depends on the thermal properties of the excitation under GSA (in this case 379 nm and 486 nm) and ESA (in this case 405 nm) matched conditions.[23,24] Therefore, all the processes described above are temperature-dependent in the 290–440 range, and it can be concluded that the $^5$D$_4$ population decreases when the temperature increases under the two excitation wavelengths that matches to GSA ($\lambda_{ex}$ = 379 nm and $\lambda_{ex}$ = 486 nm) as shown in Fig. 9b and c, respectively. In contrast, when the excitation matches to ESA ($\lambda_{ex}$ = 405 nm), the $^5$D$_4$ population increases with temperature as depicted in Fig. 9a. The opposing thermal dependence of the $^5$D$_4$–$^7$F$_5$ transition under GSA and ESA excitation wavelengths supported our hypothesis that the FIR of those signals in a single emission band can be calibrated with temperature for SBR thermometry. The FIR is defined as follows (eqn (4)):

$$\text{FIR} = \frac{I(\text{ESA})}{I(\text{GSA})} \tag{4}$$

wherein $I$ represent the intensity ratio of the green emission of Tb$^{3+}$ which corresponds to the transition $^5$D$_4 \rightarrow {}^7$F$_5$.



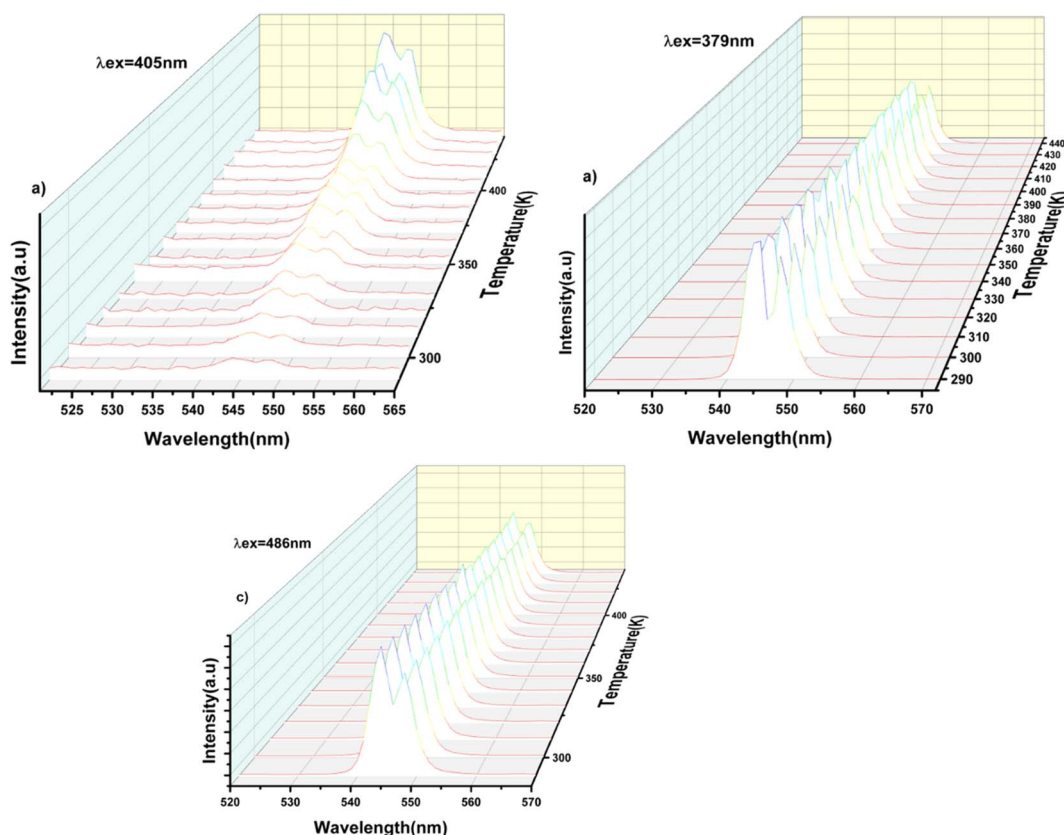**Fig. 9** Emission spectra of the LSGW:0.3Tb$^{3+}$ phosphor at different temperatures at: (a) 405 nm excitation (ESA), (b) 379 nm (GSA), (c) 486 nm (GSA).

Specifically, for both FIR1 ($I_{ex}(405)/I_{ex}(379$ nm)) and FIR2 ($I_{ex}(405)/I_{ex}(486$ nm)) the value of FIR increased rapidly from 0.02 to 0.6 when the temperature increased from 290 to 440 K as depicted in Fig. 10. In order to quantify the thermal sensing performance, the absolute (eqn (5)) and relative (eqn (6)) thermal sensitivities were calculated using the following equations:[25,26]

$$S_a = \frac{dFIR}{dT} \qquad (5)$$

$$S_r = \frac{1}{FIR}\frac{dFIR}{dT} \qquad (6)$$

where dFIR is the change in the FIR value as a result of a temperature change $\delta T$. Fig. 11a shows $S_{a1}$ and $S_{a2}$ as a function of temperature. ($S_{a1}$) and ($S_{a2}$) reached their maximum value of about 0.0089 $K^{-1}$ and 0.011 $K^{-1}$, respectively, at 440 K. Notably, the computed $S_{r1}$ and $S_{r2}$ achieved the maximum values of around 3.56% $K^{-1}$ and 4.21% $K^{-1}$ at 290 K, respectively (see Fig. 11b). These results show that the thermal sensitivities when the sample is excited at 488 nm are higher than those obtained when the sample was excited at 375 nm. It is important to note that by changing the excitation wavelength it has an impact on SBR thermometry. The LSGW:$0.3Tb^{3+}$ phosphor has a positive impact on the thermometric performance of the SBR-based luminescence thermometry, according to all of these results from the two GSA excitations (379 and 486 nm). We obtained a $S_r$ value that is among the greatest values obtained for lanthanide ions utilizing the SBR approach. Table 3 provides a number of typical FIR-based temperature sensors based in SBR thermometry technique that have been doped with various $Ln^{3+}$. In addition, the measurement error called also temperature resolution ($\delta T$) of the optical thermometer, which is relevant in practical applications, was determined using the following equation (eqn (7)):[27,28]

$$\delta_T = \frac{1}{S_r}\frac{\delta FIR}{FIR} \qquad (7)$$

wherein $\delta FIR$ is the resolution limit of the thermometric parameter, which is the minimum change in ratio that may be imposed experimentally. The limit of resolution depends on the performance of the thermometer, but is also affected by the setup of the experiment.[29,30] In order to enhance the resolution limit, it may be necessary to use better acquisition methods as well as improve measurement performance, such as extending integration time and using the average of successive measurements to reduce the experimental noise. $Tb^{3+}$ doped LSGW was measured 20 times under similar conditions at room temperature, and the results are shown in Fig. 12a and b. FIR uncertainty ($\delta FIR$) was calculated as the statistical distribution's standard deviation, which were 0.025 and 0.0316 for FIR1 (405/379) and FIR2 (405/486). Using eqn (5), Fig. 12c show that $\delta T_1 = 0.68$ K and $\delta T_2 = 0.75$ K for $T = 290$ K. When the temperature increases to 440 K, the temperature resolution increases to 1.6 K and 1.7 K for FIR1 and FIR2, respectively.



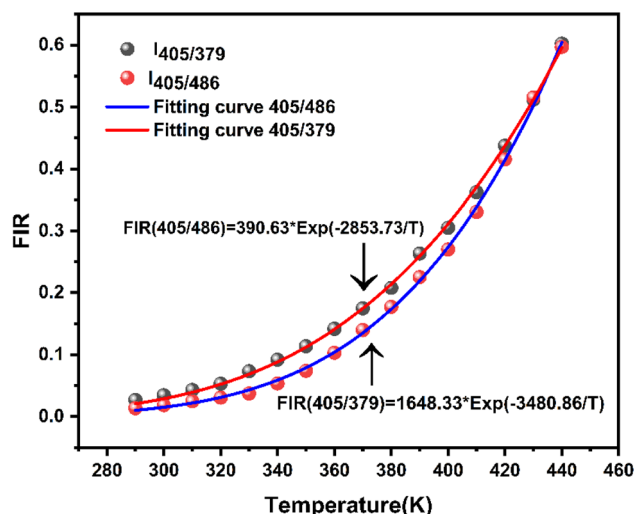Fig. 10 Luminescence intensity ratio (FIR) of the LSGW:$0.3Tb^{3+}$ phosphor in the 290−440 K temperature range for FIR1 (405/379), and FIR2 (405/486).
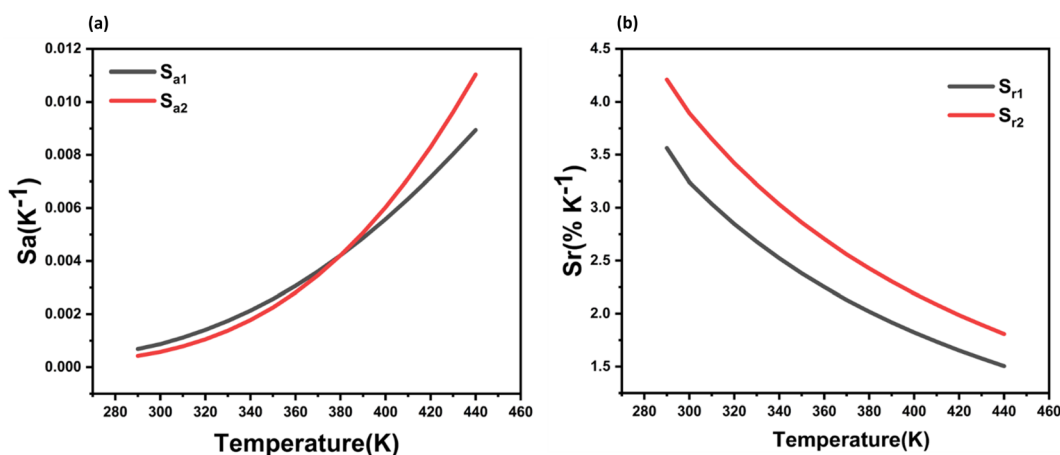


Fig. 11 (a) Absolute and, (b) relative thermal sensitivities obtained for the LSGW:$0.3Tb^{3+}$ phosphor in the 290−440 K temperature range.

**Table 3** Comparison of relative thermal sensitivity using the SBR strategy in various hosts and doped phosphors

| Host material | Emission wavelength (nm) | 1st $\lambda_{exc}$ [nm] | 2nd $\lambda_{exc}$ [nm] | $S_r$ max [% K$^{-1}$] | Ref. |
|---|---|---|---|---|---|
| KLaP$_4$O$_{12}$:Tb$^{3+}$ | 544 | 377 | 413 | 3.2 | 31 |
| Oxyfluorotellurite glass:Tb$^{3+}$ | 543 | 377 | 413 | 2.05 | 24 |
| KGdW$_4$O$_8$:Tb$^{3+}$ | 543 | 377 | 413 | 1.63 | 32 |
| CaWO$_4$:Tb$^{3+}$ | 544 | 300 | 380 | 1.28 | 33 |
| CaWO$_4$:Tb$^{3+}$ | 544 | 310 | 378 | 1.6 | 34 |
| YVO$_4$:Er$^{3+}$ | 552 | 350 | 379 | 2.34 | 35 |
| YVO$_4$:Er$^{3+}$ | 552 | 350 | 489 | 2.61 | 35 |
| LiLaP$_4$O$_{12}$:Eu$^{3+}$ | 590 | 450 | 620 | 2.17 | 36 |
| LiLaP$_4$O$_{12}$:Eu$^{3+}$ | 590 | 450 | 650 | 2.31 | 36 |
| LiLaP$_4$O$_{12}$:Eu$^{3+}$ | 590 | 450 | 690 | 1.9 | 36 |
| Lu$_2$O$_3$:Eu$^{3+}$ | 590 | 586.5 | 611 | 0.93 | 37 |
| LaPO$_4$:Nd$^{3+}$ | 890 | 808 | 1064 | 4.35 | 38 |
| LaPO$_4$:Nd$^{3+}$ | 890 | 808 | 1064 | 3.04 | 38 |
| LaPO$_4$:Nd$^{3+}$ | 890 | 808 | 1064 | 7.19 | 38 |
| LSGW:Tb$^{3+}$ | 545 | 405 | 486 | 4.2 | This work |
| LSGW:Tb$^{3+}$ | 545 | 405 | 379 | 3.56 | This work |

To verify the precision of the employed temperature sensing methods, the determined thermometric parameters (FIR values) were meticulously measured through successive cycles of the sample between ambient temperature (290 K) and elevated temperatures (440 K), as illustrated in Fig. 13. The calculation used to ascertain the repeatability ($R$) was as follows:[39,40]
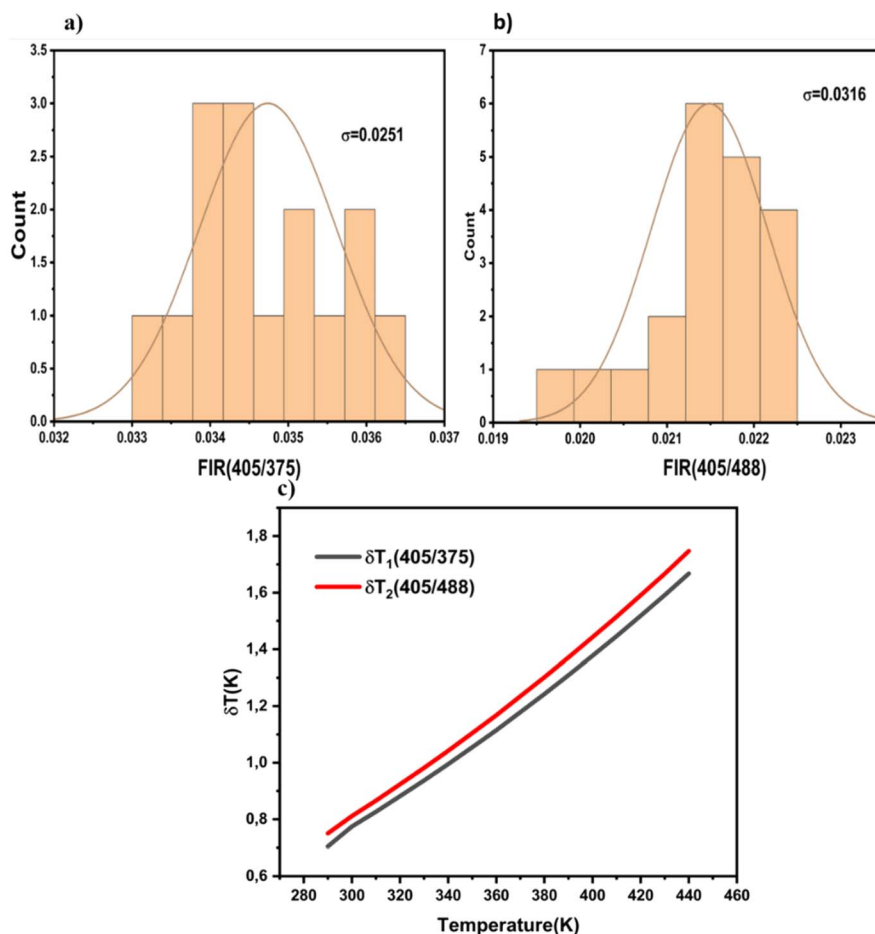


**Fig. 12** Standard deviations at *RT* for (a) FIR1 and (b) FIR2 obtained after 20 measurements at 300 K. (c) Temperature resolution values for FIR1 ($\delta T_1$) and FIR2 ($\delta T_2$).
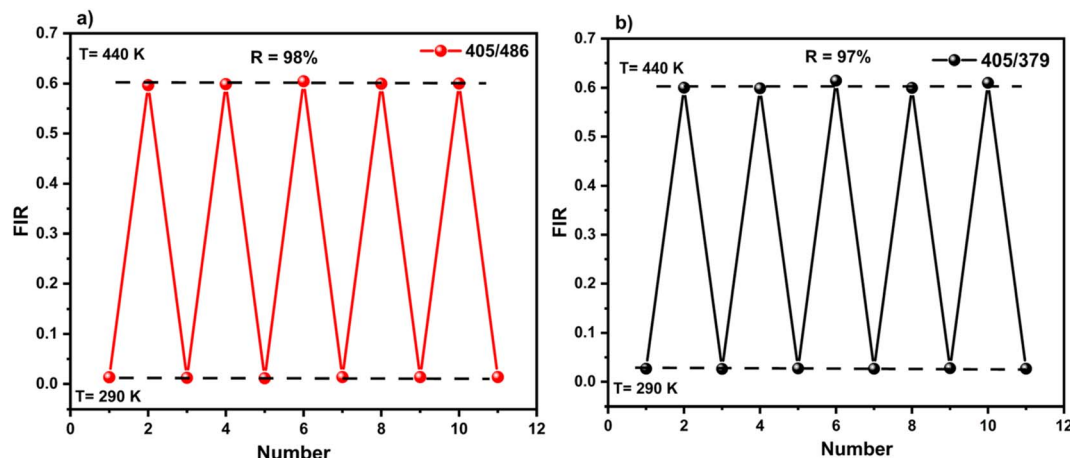
**Fig. 13** Repeatability assessment ($R$) (a) 405/486 (b) 405/379 for LSGW:0.3Tb$^{3+}$ phosphors.

$$R_{\mathrm{p}}(100\%) = \left( 1 - \frac{\max\left| M_{\mathrm{i}}(T)_{\mathrm{c}} \times M(T)_{\mathrm{c}} \right|}{\mathrm{FIR}_{\mathrm{c}}} \right) \times 100$$

where $M_{\mathrm{i}}(T)_{\mathrm{c}}$ represents the measured parameter (FIR) in the i$^{\mathrm{th}}$ cycle and $M(T)_{\mathrm{c}}$ over 10 cycles. The determined FIR values exhibit reversible changes with temperature, with the FIR values for 405/486 and 405/379 being 98% and 97%, respectively, within the measured temperature range. This confirms the excellent repeatability and reliability of the employed thermometric methods.

## 5. Conclusions

The XRD and Rietveld refinement analyses reveal that LSGW:Tb$^{3+}$ crystallizes in the tetragonal system with the $I4_1/a$ space group. SEM examination was employed to assess the phosphors' morphology, indicating a particle size of 30 μm. Absorption measurements confirm the formation of the tungstate host, with the distinct WO$_4^{2-}$ groups' absorption bands observed in the visible spectrum. By employing two Fluorescence Intensity Ratio (FIR) parameters for the 544 nm green emission, excited firstly at 405 nm, and 379 nm, and then at 405 nm, and 488 nm, for both ground state absorption (GSA) and excited state absorption (ESA), the $S_{\mathrm{r}}$ relative thermal sensitivity of the luminescent thermometer peaks at 3.56% K$^{-1}$ and 4.21% K$^{-1}$, respectively, at 290 K within the temperature range of 290–440 K. We evaluated their suitability for single-band ratiometric (SBR) luminescent thermometry. Notably, the modulation of relative sensitivity in this thermometry through a simple change in excitation wavelength was demonstrated. The highest relative sensitivities, were achieved for 405 nm and 488 nm excitations. The temperature resolution ($\delta T$) of the luminescent thermometer is calculated to be $\delta T_1 = 0.68$ K and $\delta T_2 = 0.75$ K for $T = 290$ K, respectively. Our study contributes to the understanding of LSGW:Tb$^{3+}$ as a promising candidate for precise temperature measurements and opens avenues for further exploration in luminescent sensing applications.

## Conflicts of interest

There are no conflicts to declare.

## References

1 D. Jaque and F. Vetrone, Luminescence nanothermometry, *Nanoscale*, 2012, **4**, 4301–4326, DOI: **10.1039/c2nr30764b**.

2 K. Trejgis, R. Lisiecki, A. Bednarkiewicz and L. Marciniak, Nd$^{3+}$ doped TZPN glasses for NIR operating single band ratiometric approach of contactless temperature readout, *J. Lumin.*, 2020, **224**, 117295, DOI: **10.1016/j.jlumin.2020.117295**.

3 A. S. Souza, L. A. O. Nunes, I. G. N. Silva, F. A. M. Oliveira, L. L. da Luz, H. F. Brito, M. C. F. C. Felinto, R. A. S. Ferreira, S. A. Júnior, L. D. Carlos and O. L. Malta, Highly-sensitive Eu$^{3+}$ ratiometric thermometers based on excited state absorption with predictable calibration, *Nanoscale*, 2016, **8**, 5327–5333, DOI: **10.1039/c6nr00158k**.

4 J. Drabik, R. Kowalski and L. Marciniak, Enhancement of the sensitivity of single band ratiometric luminescent nanothermometers based on Tb$^{3+}$ ions through activation of the cross relaxation process, *Sci. Rep.*, 2020, **10**, 11190, DOI: **10.1038/s41598-020-68145-5**.

5 J. Meng, H. Fang, H. Wang, Y. Wu, C. Wei, S. Li, X. Geng, X. Li, J. Zhang, G. Wen and P. Wang, Effects of refractory metal additives on diboride-based ultra-high temperature ceramics: a review, *Int. J. Appl. Ceram. Technol.*, 2023, **20**, 1350–1370, DOI: **10.1111/ijac.14336**.

6 J. Wang, H. Yu, Y. Wu and R. Boughton, Recent developments in functional crystals in china, *Engineering*, 2015, **1**, 192–210.

7 Y. Kalisky, L. Kravchik and C. Labbe, Repetitive modulation and passively Q-switching of diode-pumped Nd–KGW laser, *Opt. Commun.*, 2001, **189**, 113–125.

8 P. Cerny, H. Jelinkova, T. T. Basiev and P. G. Zverev, Properties of transient and steady-state stimulated Raman scattering in KGd(WO$_4$)$_2$ and BaWO$_4$ tungstate crystals, in

*Growth Fabr. Devices Appl. Laser Nonlinear Mater*, SPIE, 2001, pp. , pp. 101–108, https://www.spiedigitallibrary.org/conference-proceedings-of-spie/4268/0000/Properties-of-transient-and-steady-state-stimulated-Raman-scattering-in/10.1117/12.424630.short, accessed December 15, 2023.

9 C. S. Lim, V. V. Atuchin, A. S. Aleksandrovsky and M. S. Molokeev, Preparation of NaSrLa(WO$_4$)$_3$:Ho$^{3+}$/Yb$^{3+}$ ternary tungstates and their upconversion photoluminescence properties, *Mater. Lett.*, 2016, **181**, 38–41.

10 B. Xiao, Y. Huang, L. Zhang, Z. Lin and G. Wang, Growth, structure and spectroscopic characterization of Nd$^{3+}$-doped KBaGd(WO$_4$)$_3$ crystal with a disordered structure, *PLoS One*, 2012, 7, e40229.

11 K. Zhong, H. Ye, X. Wang, Y. Li and X. Yao, Synthesis and photoluminescence properties of a novel red-emitting Eu$^{3+}$-doped LiSrGd(WO$_4$)$_3$ phosphors, *J. Mater. Sci. Mater. Electron.*, 2021, **32**, 17170–17181, DOI: 10.1007/s10854-021-06176-y.

12 T. A. Para and S. K. Sarkar, Challenges in Rietveld refinement and structure visualization in ceramics, *Adv. Ceram. Mater.*, 2021, DOI: 10.5772/INTECHOPEN.96065.

13 F. Ben Bacha, S. Megdiche Borchani, M. Dammak and M. Megdiche, Optical and complex impedance analysis of double tungstates of mono- and trivalent metals for LiGd(WO$_4$)$_2$ compound, *J. Alloys Compd.*, 2017, **712**, 657–665, DOI: 10.1016/j.jallcom.2017.04.107.

14 K. Baishya, J. S. Ray, P. Dutta, P. P. Das and S. K. Das, Graphene-mediated band gap engineering of WO$_3$ nanoparticle and a relook at Tauc equation for band gap evaluation, *Appl. Phys. A*, 2018, **124**, 704, DOI: 10.1007/s00339-018-2097-0.

15 Z. Wang, Y. Wang, Y. Li and B. Liu, Low Dimensional Effects on Luminescent Properties of CaWO$_4$:Tb Nanophosphor, *J. Electrochem. Soc.*, 2010, **157**, J125, DOI: 10.1149/1.3309727.

16 Y. Li, Z. Wang, L. Sun, Z. Wang, S. Wang, X. Liu and Y. Wang, Investigation of oxygen vacancy and photoluminescence in calcium tungstate nanophosphors with different particle sizes, *Mater. Res. Bull.*, 2014, **50**, 36–41, DOI: 10.1016/j.materresbull.2013.10.022.

17 Y. Li and G. Hong, Synthesis and luminescence properties of nanocrystalline Gd$_2$O$_3$:Eu$^{3+}$ by combustion process, *J. Lumin.*, 2007, **124**, 297–301, DOI: 10.1016/j.jlumin.2006.03.016.

18 K. Trejgis, A. Bednarkiewicz and L. Marciniak, Engineering excited state absorption based nanothermometry for temperature sensing and imaging, *Nanoscale*, 2020, **12**, 4667–4675, DOI: 10.1039/c9nr09740f.

19 Q. Liu, M. Zhang, Z. Ye, X. Wang, Q. Zhang and B. Wei, Structure variation and luminescence enhancement of BaLaMg(Sb, Nb)O$_6$:Eu$^{3+}$ double perovskite red phosphors based on composition modulation, *Ceram. Int.*, 2019, **45**, 7661–7666, DOI: 10.1016/j.ceramint.2019.01.065.

20 F. Ayachi, K. Saidi, W. Chaabani and M. Dammak, Synthesis and luminescence properties of Er$^{3+}$ doped and Er$^{3+}$–Yb$^{3+}$ codoped phosphovanadate YP$_{0.5}$V$_{0.5}$O$_4$ phosphors, *J. Lumin.*, 2021, **240**, 118451, DOI: 10.1016/j.jlumin.2021.118451.

21 D. L. Dexter and J. H. Schulman, Theory of Concentration Quenching in Inorganic Phosphors, *J. Chem. Phys.*, 2004, **22**, 1063–1070, DOI: 10.1063/1.1740265.

22 Y. Tian, Y. Fang, B. Tian, C. Cui, P. Huang, L. Wang, H. Jia and B. Chen, Molten salt synthesis, energy transfer, and temperature quenching fluorescence of green-emitting β-Ca$_2$P$_2$O$_7$:Tb$^{3+}$ phosphors, *J. Mater. Sci.*, 2015, **50**, 6060–6065, DOI: 10.1007/s10853-015-9155-1.

23 Z. E. A. A. Taleb, K. Saidi, M. Dammak, D. Przybylska and T. Grzyb, Ultrasensitive optical thermometry using Tb$^{3+}$ doped NaSrGd(MoO$_4$)$_3$ based on single band ratiometric luminescence, *Dalton Trans.*, 2023, **52**, 4954–4963, DOI: 10.1039/d3dt00376k.

24 J. Drabik, R. Lisiecki and L. Marciniak, Optimization of the thermometric performance of single band ratiometric luminescent thermometer based on Tb$^{3+}$ luminescence by the enhancement of thermal quenching of GSA-excited luminescence in TZPN glass, *J. Alloys Compd.*, 2021, **858**, 157690, DOI: 10.1016/j.jallcom.2020.157690.

25 A. K. Singh, S. K. Singh, B. K. Gupta, R. Prakash and S. B. Rai, Probing a highly efficient dual mode: down-upconversion luminescence and temperature sensing performance of rare-earth oxide phosphors, *Dalton Trans.*, 2013, **42**, 1065–1072, DOI: 10.1039/c2dt32054a.

26 F. Ayachi, K. Saidi, M. Dammak, W. Chaabani, I. Mediavilla-Martínez and J. Jiménez, Dual-mode luminescence of Er$^{3+}$/Yb$^{3+}$ codoped LnP$_{0.5}$V$_{0.5}$O$_4$ (Ln = Y, Gd, La) for highly sensitive optical nanothermometry, *Mater. Today Chem.*, 2023, **27**, 101352, DOI: 10.1016/j.mtchem.2022.101352.

27 K. Saidi, M. Dammak, K. Soler-Carracedo and I. R. Martín, A novel optical thermometry strategy based on emission of Tm$^{3+}$/Yb$^{3+}$ codoped Na$_3$GdV$_2$O$_8$ phosphors, *Dalton Trans.*, 2022, **51**, 5108–5117, DOI: 10.1039/d1dt03747a.

28 I. Kachou, K. Saidi, R. Salhi and M. Dammak, Synthesis and optical spectroscopy of Na$_3$Y(VO$_4$)$_2$:Eu$^{3+}$ phosphors for thermometry and display applications, *RSC Adv.*, 2022, **12**, 7529–7539, DOI: 10.1039/d2ra00539e.

29 C. D. S. Brites, A. Millán and L. D. Carlos, *Handbook on the Physics and Chemistry of Rare Earths*, Actin, 2016, vol. 49, pp. 339–427.

30 K. Soler-Carracedo, I. R. Martín, F. Lahoz, H. C. Vasconcelos, A. D. Lozano-Gorrín, L. L. Martín and F. Paz-Buclatin, Er$^{3+}$/Ho$^{3+}$ codoped nanogarnet as an optical FIR based thermometer for a wide range of high and low temperatures, *J. Alloys Compd.*, 2020, **847**, 156541, DOI: 10.1016/j.jallcom.2020.156541.

31 J. Drabik, R. Kowalski and L. Marciniak, Enhancement of the sensitivity of single band ratiometric luminescent nanothermometers based on Tb$^{3+}$ ions through activation of the cross relaxation process, *Sci. Rep.*, 2020, **10**, 11190.

32 J. Stefanska, M. Chrunik and L. Marciniak, Sensitivity Enhancement of the Tb$^{3+}$-Based Single Band Ratiometric Luminescent Thermometry by the Metal-to-Metal Charge Transfer Process, *J. Phys. Chem. C*, 2021, **125**, 5226–5232, DOI: 10.1021/acs.jpcc.0c11631.

33 L. Li, F. Qin, L. Li, H. Gao and Z. Zhang, New Strategy for Circumventing the Limitation of Thermally Linked States and Boosting the Relative Thermal Sensitivity of Luminescence Ratiometric Thermometry, *J. Phys. Chem. C*, 2019, **123**, 6176–6181, DOI: 10.1021/acs.jpcc.8b12175.

34 L. Li, F. Qin, L. Li, H. Gao and Z. Zhang, New Strategy for Circumventing the Limitation of Thermally Linked States and Boosting the Relative Thermal Sensitivity of Luminescence Ratiometric Thermometry, *J. Phys. Chem. C*, 2019, **123**, 6176–6181, DOI: 10.1021/acs.jpcc.8b12175.

35 I. E. Kolesnikov, D. V. Mamonova, M. A. Kurochkin, E. Yu. Kolesnikov and E. Lähderanta, Multimode luminescence thermometry based on emission and excitation spectra, *J. Lumin.*, 2021, **231**, 117828, DOI: 10.1016/j.jlumin.2020.117828.

36 K. Trejgis, A. Bednarkiewicz and L. Marciniak, Engineering excited state absorption based nanothermometry for temperature sensing and imaging, *Nanoscale*, 2020, **12**, 4667–4675.

37 A. Ćirić, I. Zeković, M. Medić, Ž. Antić and M. D. Dramićanin, Judd-Ofelt modelling of the dual-excited single band ratiometric luminescence thermometry, *J. Lumin.*, 2020, **225**, 117369.

38 K. Trejgis, K. Maciejewska, A. Bednarkiewicz and L. Marciniak, Near-Infrared-to-Near-Infrared Excited-State Absorption in $LaPO_4$:$Nd^{3+}$ Nanoparticles for Luminescent Nanothermometry, *ACS Appl. Nano Mater.*, 2020, **3**, 4818–4825, DOI: 10.1021/acsanm.0c00853.

39 Z. Wang, M. Jia, M. Zhang, X. Jin, H. Xu and Z. Fu, Trimodal Ratiometric Luminescent Thermometer Covering Three Near-Infrared Transparency Windows, *Inorg. Chem.*, 2021, **60**, 14944–14951, DOI: 10.1021/acs.inorgchem.1c02311.

40 Z. E. A. A. Taleb, K. Saidi and M. Dammak, Dual-mode optical ratiometric thermometry using $Pr^{3+}$-doped NaSrGd $(MoO_4)_3$ phosphors with tunable sensitivity, *Dalton Trans.*, 2023, **52**, 18069–18081.